

C^1 conforming quadrilateral finite elements with complete second-order derivatives on vertices and its application to Kirchhoff plates

WU Yang, XING YuFeng ^{*} & LIU Bo

Institute of Solid Mechanics, Beihang University, Beijing 100191, China

Received June 13, 2019; accepted September 17, 2019; published online January 20, 2020

The classical problem of the construction of C^1 conforming single-patch quadrilateral finite elements has been solved in this investigation by using the blending function interpolation method. In order to achieve the C^1 conformity on the interfaces of quadrilateral elements, complete second-order derivatives are used at the element vertices, and the information of geometrical mapping is also considered into the construction of shape functions. It is found that the shape functions and the polynomial spaces of the present elements vary with element shapes. However, the developed quadrilateral elements are at least third order for general quadrilateral shapes and fifth order for rectangular shapes. Therefore, very fast convergence can be achieved. A promising feature of the present elements is that they can be used in cooperation with those high-precision rectangular and triangular elements. Since the present elements are over conforming on element vertices, an approach for handling problems of material discontinuity is also proposed. Numerical examples of Kirchhoff plates are employed to demonstrate the computational performance of the present elements.

finite element method, quadrilateral elements, C^1 conforming, Kirchhoff plates

Citation: Wu Y, Xing Y F, Liu B. C^1 conforming quadrilateral finite elements with complete second-order derivatives on vertices and its application to Kirchhoff plates. *Sci China Tech Sci*, 2020, 63, <https://doi.org/10.1007/s11431-019-1448-6>

1 Introduction

It is well known that the finite element method (FEM) is one of the most powerful numerical methods in solving problems in engineering and scientific community. Since its beginning in 1950s, enormous finite elements have been developed for different problems. Classified by the continuity of the field variables, the existing finite elements can be roughly divided into two categories—the family of C^0 elements that require the continuity of field variable only and the C^1 elements that require the continuity of both field variable and its first-order derivatives (note that the finite element method with higher-order continuity are also studied by researchers [1–3]). It is fair to say that the most widely used finite elements in

commercial software are still the C^0 type. Due to its simplicity of conformity requirement, elements in different shapes can be easily constructed based on the concept of isoparametric mapping. However, for problems such as Kirchhoff plates and shells [4], couple stress/strain gradient elasticity [5], and divergence-free velocity approximations for steady Stokes problem [6], the C^1 conformity of the field variables is required. Unfortunately, it is not an easy task to construct the C^1 finite elements, especially the quadrilateral ones.

Regardless of its long history of research, the C^1 finite elements are still far from fully developed. Most of the existing C^1 elements are of triangular shapes, such as the Hsieh-Clough-Tocher (HCT) macro-triangle [7], the Argyris triangles (TUBA family) [8], and the reduced Bell triangle [9]. Only a few arbitrarily quadrilateral C^1 conforming elements

*Corresponding author (email: xingyf@buaa.edu.cn)

were developed by Clough and Felippa [10], and Fraeijs de Veubeke [11] in the early times. As shown in Figure 1, these elements are in fact composed of 12 and 4 cubic triangular elements. For this reason, they are also named as macro elements by researchers [6,12]. The constructing process of these elements is very similar to the HCT triangle elements, where part of the degrees-of-freedom (DOFs) must be condensed firstly to satisfy the C^1 continuity on the interfaces of internal triangles. As pointed out in ref. [13], the accuracy of Clough's quadrilateral elements rapidly deteriorates with the increase of aspect ratios because subdivision may introduce angles very closed to π , causing ill-conditioning, while the situation is better for Fraeijs de Veubeke's elements. Using Fraeijs de Veubeke's subdivision method and the cubic spline Hermite interpolation, Chen and Li [14] reconstructed two conforming quadrilateral elements, and numerical examples proved that their elements are less sensitive to mesh distortion.

The remaining conforming quadrilateral elements are mainly the rectangular ones, such as the well-known bicubic Borgner-Fox-Schmit (BFS) elements [15]. This element is easily performed since the shape functions are obtained by tensor product of cubic Hermite polynomials. However, the conformity is only ensured when the element edges parallel to the axes of global coordinates. Some researchers [16] applied it to the quadrilateral shapes, however, it found that the convergence rate is poor due to the loss of C^1 conformity. Other conforming rectangular elements were proposed by Gopalacharyulu [17] and Watkins [18]. Similar to the TUBA elements, complete second-order derivatives were used as vertex DOFs. Therefore, these rectangular elements can be used corporately with TUBA elements [8]. Because of the use of high-order approximation, fast convergence were achieved [18,19]. For these reasons, these rectangular elements along with the TUBA triangular elements are generally named as high-precision elements in refs. [20,21]. Unfortunately, the rectangular elements cannot be used with arbitrarily quadrilateral shapes, otherwise the C^1 conformity will be violated. For a comprehensive review of the early C^1 elements, one can refer to ref. [22].

Even though it is difficult to construct the quadrilateral C^1 conforming elements, they are important in modeling com-

plicated domains with structured and unstructured meshes. Compared with the non-conforming C^1 elements [23,24] and the hybrid elements [25], the C^1 conforming elements use simpler displacement-variational principle and their results often exhibit good convergence and upper-bound properties. Besides, quadrilateral elements are generally more accurate than triangular elements. However, it seems little progress has been made on the construction of quadrilateral elements since 1980s [22]. In recent literatures, the application of C^1 finite elements is still limited on the early developed rectangular elements [6,19,26,27], triangular elements [28,29], and the subdivided quadrilateral elements [6,12,30]. As the aforementioned advantages of C^1 conforming quadrilateral elements and the ill-conditioning problems of existing subdivided quadrilateral elements, the “real” single-patch, i.e. non-subdivided, C^1 conforming finite elements are urgently expected to be constructed, which is one of motivations of the present work.

In the early times, attempts had been made to construct C^1 conforming quadrilateral elements with the usage of only kinematic DOFs, i.e. the deflection w and rotations w_x, w_y . As pointed out in refs. [25,31], it is impossible to construct such a strictly C^1 conforming three-node triangular and four-node quadrilateral elements using polynomial interpolation along with w, w_x, w_y per node. In fact, constructing C^1 quadrilateral elements requires all second-order derivatives at vertices. This situation was indeed realized by many researchers [4,10]. However, to the best knowledge of the authors, the corresponding elements are still unavailable in literatures. There are probably two main reasons. First, the conforming elements with high-order derivatives as unknowns have long been thought to be unable to account for strain discontinuity (or material discontinuity) [32,33]. This “limitation” may discourage researchers to construct relevant elements. However, as pointed out in ref. [31], it is possible to solve this problem by transforming the nodal variables to be normal and tangential to the interfaces and relaxing the continuity on the parameters $\partial^2 w / \partial n^2$. Second, as it is shown in this work, the shape functions for this kind of quadrilateral elements should not be constructed from a fixed polynomial space, because the polynomial space is influenced by the element shape when satisfying the requirement of C^1 conformity. This may be the main reason that was not realized by researchers.

In this context, we develop two types of C^1 conforming quadrilateral elements, named CQ24 and CQ28 elements with smooth polynomial expansion using the blending function interpolation method. Complete second-order derivatives are used as the vertex DOFs, and a remedy for modeling problems with material discontinuity is also proposed. Besides the aforementioned advantages of C^1 conforming quadrilateral elements, another promising feature of the present elements is that they can be used cooperatively

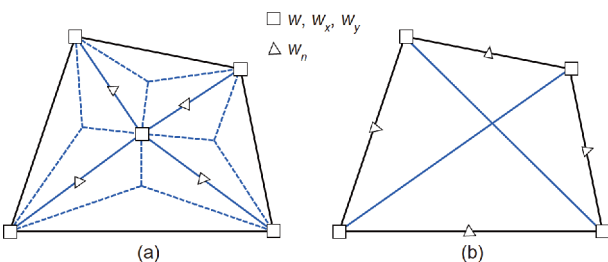


Figure 1 (Color online) Conforming quadrilateral elements. (a) Proposed by Clough and Felippa; (b) proposed by Fraeijs de Veubeke.

with the high-precision rectangular [18] and triangular elements [8]. Therefore, the present elements are a significant complement to this family of high-precision C^1 conforming elements. Despite that the high-order derivatives are nodal unknowns, the present elements might be the simplest kind of C^1 conforming quadrilateral elements with polynomial solution spaces.

2 The Hermite blending function interpolation

The Hermite blending function interpolation method was formulated by Gordon [34], and it was used later by Watkins [18] to develop the C^1 conforming rectangular elements. This method is also used in this work to derive the FEM displacement field of present elements, so it is included here for completeness. As shown in Figure 2(a), consider a smooth function $w(\xi, \eta)$ defined on a unit square domain $U=[0, 1] \times [0, 1]$ in ξ - η coordinates. The boundary values and normal derivatives of w on the four sides are denoted by f_i and g_i , $i=1, 2, 3, 4$, i.e.,

$$\begin{aligned} f_1(\xi) &= w(\xi, 0), f_2(\eta) = w(1, \eta), \\ f_3(\xi) &= w(\xi, 1), f_4(\eta) = w(0, \eta), \\ g_1(\xi) &= w_\eta(\xi, 0), g_2(\eta) = w_\xi(1, \eta), \\ g_3(\xi) &= w_\eta(\xi, 1), g_4(\eta) = w_\xi(0, \eta), \end{aligned} \quad (1)$$

where w_ξ and w_η denote the first-order partial derivatives with respect to ξ and η . The blending function interpolation is to find an approximation function $\tilde{w}(\xi, \eta)$ which has the same boundary values and normal derivatives as w . To this end, the following 3rd-order Hermite interpolation bases at $[0, 1]$ are selected as the blending functions

$$\begin{aligned} h_1(\xi) &= (1-\xi)^2(1+2\xi), h_2(\xi) = \xi(1-\xi)^2, \\ h_3(\xi) &= \xi^2(3-2\xi), h_4(\xi) = \xi^2(\xi-1). \end{aligned} \quad (2)$$

$$\begin{aligned} P_\xi[w] &= g_4(\eta)h_1(\xi) + f_4(\eta)h_2(\xi) + f_2(\eta)h_3(\xi) + g_2(\eta)h_4(\xi), \\ P_\eta[w] &= g_1(\xi)h_1(\eta) + f_1(\xi)h_2(\eta) + f_3(\xi)h_3(\eta) + g_3(\xi)h_4(\eta), \end{aligned}$$

$$\begin{aligned} P_\xi P_\eta[w] &= \left[g'_1(0)h_1(\eta) + f'_1(0)h_2(\eta) + f'_3(0)h_3(\eta) + g'_3(0)h_4(\eta) \right] h_1(\xi) \\ &\quad + \left[g_1(0)h_1(\eta) + f_1(0)h_2(\eta) + f_3(0)h_3(\eta) + g_3(0)h_4(\eta) \right] h_2(\xi) \\ &\quad + \left[g_1(1)h_1(\eta) + f_1(1)h_2(\eta) + f_3(1)h_3(\eta) + g_3(1)h_4(\eta) \right] h_3(\xi) \\ &\quad + \left[g'_1(1)h_1(\eta) + f'_1(1)h_2(\eta) + f'_3(1)h_3(\eta) + g'_3(1)h_4(\eta) \right] h_4(\xi). \end{aligned} \quad (9)$$

Using the interpolation method in eq. (8), one can construct a two dimensional function \tilde{w} with prescribed boundary functions f_i and g_i . This is the main idea for the construction of element displacement functions of the present elements. We note that the blending function interpolation is valid only when w is sufficiently smooth, which means the boundary functions should be consistent enough.

where h_1, h_3 are related to the end function values and h_2, h_4 are related to the first-order derivatives at two ends. By interpolating w along ξ direction, see Figure 2(b), one can obtain:

$$\begin{aligned} P_\xi[w] &= g_4(\eta)h_1(\xi) + f_4(\eta)h_2(\xi) + f_2(\eta)h_3(\xi) \\ &\quad + g_2(\eta)h_4(\xi), \end{aligned} \quad (3)$$

where $P_\xi[\bullet]$ is the projection operator [34] related to ξ direction. It follows that $P_\xi[w]$ has the same boundary values and normal derivatives as w on edges $\xi=0$ and 1. So the interpolation residual R defined by

$$R = w - P_\xi[w] \quad (4)$$

has zero values and zero normal derivatives on edges $\xi=0$ and 1. By interpolating R in η direction, see Figure 2(c), one can obtain:

$$\begin{aligned} P_\eta[R] &= R(\xi, 0)h_1(\eta) + R_\eta(\xi, 0)h_2(\eta) + R(\xi, 1)h_3(\eta) \\ &\quad + R_\eta(\xi, 1)h_4(\eta), \end{aligned} \quad (5)$$

where $P_\eta[\bullet]$ is the projection operator with respect to η direction; R_ξ, R_η are the two partial derivatives of R . Clearly, $P_\eta[R]$ also has zero values and normal derivatives on $\eta=0$ and 1, while the values and normal derivatives on $\eta=0$ and 1 are the same as R . Finally, one can conclude that

$$\tilde{w} = P_\xi[w] + P_\eta[R] \quad (6)$$

is the desired function that has the same boundary values and normal derivatives as w . From eqs. (3) and (5), one can see that the projection operators are liner, and it follows:

$$P_\eta[R] = P_\eta[w - P_\xi[w]] = P_\eta[w] - P_\eta[P_\xi[w]]. \quad (7)$$

Note that the projection operators are also commutative [34], which implies $P_\eta[P_\xi[w]] = P_\xi[P_\eta[w]]$ or, for simplicity, $P_\eta P_\xi[w] = P_\xi P_\eta[w]$. Substituting eq. (7) into eq. (6) yields:

$$\tilde{w}(\xi, \eta) = P_\xi[w] + P_\eta[w] - P_\xi P_\eta[w], \quad (8)$$

where

For example, on the corner $(\xi=0, \eta=0)$, the given boundary functions f_i and g_i ($i=1, 2, 3, 4$) should satisfy $f_1(0)=f_4(0)$, $f'_4(0)=g_1(0)$, etc. Although the check of consistency is somewhat tedious, this difficulty does not appear in element construction of this work since the boundary functions are interpolated by nodal variables, and the consistence is satisfied automatically.

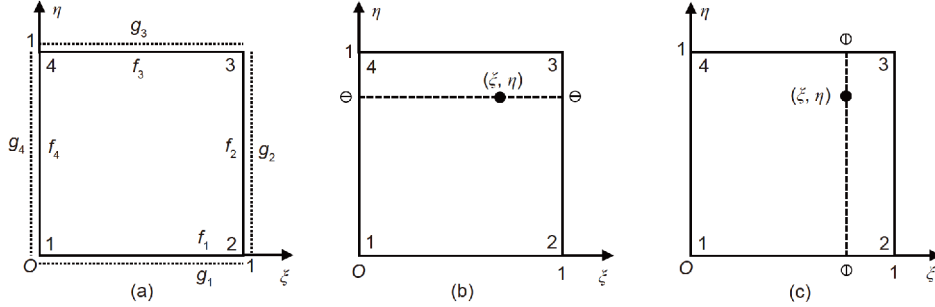


Figure 2 Blending function interpolation on a square domain. (a) Boundary functions; (b) interpolation along ξ direction; (c) interpolation along η direction.

3 Conforming quadrilateral elements: CQ24 and CQ28

In this section we determine the element displacement functions for our conforming quadrilateral elements. For better understanding of the present work, we firstly point out the problems in conventional rectangular C^1 conforming elements. The shape functions of them are generally defined in a standard squared domain in natural coordinates, and the boundary functions, i.e. f_i and g_i in eq. (1), of the displacement \tilde{w} are the polynomials of natural coordinates ξ or η .

3.1 Problems in conventional rectangular C^1 conforming elements

If the element shape is quadrilateral instead of rectangular,

$$\mathbf{J} = \begin{bmatrix} J_{11} & J_{12} \\ J_{21} & J_{22} \end{bmatrix} = \begin{bmatrix} \partial x / \partial \xi & \partial y / \partial \xi \\ \partial x / \partial \eta & \partial y / \partial \eta \end{bmatrix} = \begin{bmatrix} (x_1 - x_2 + x_3 - x_4)\eta - x_1 + x_2 \\ (x_1 - x_2 + x_3 - x_4)\xi - x_1 + x_4 \end{bmatrix}$$

which is generally non-constant but a function of ξ and η . The normal derivatives of \tilde{w} on element boundaries can be expressed by

$$\tilde{w}_n = n_x \tilde{w}_x + n_y \tilde{w}_y, \quad (13)$$

where n_x, n_y are the cosines of normal direction, which are constants for each element boundary; \tilde{w}_x, \tilde{w}_y are the partial derivatives of \tilde{w} with respect to global coordinates, and they can be expressed as

$$\begin{bmatrix} \tilde{w}_x \\ \tilde{w}_y \end{bmatrix} = \frac{1}{\det|\mathbf{J}|} \begin{bmatrix} J_{22} & -J_{12} \\ -J_{21} & J_{11} \end{bmatrix} \begin{bmatrix} \tilde{w}_\xi \\ \tilde{w}_\eta \end{bmatrix}, \quad (14)$$

where $\tilde{w}_\xi, \tilde{w}_\eta$ can be directly expressed by the boundary functions f_i and g_i . For example, on edge $\eta=0$, there are $\tilde{w}_\xi = f'_1(\xi)$ and $\tilde{w}_\eta = g_1(\xi)$, refer to Figure 2, that is, \tilde{w}_ξ and \tilde{w}_η are the polynomials of the ξ - η coordinates or the length coordinate s because of the linear mapping between ξ - η and s . However, \tilde{w}_x, \tilde{w}_y on element boundaries may not be polynomials of s for general quadrilateral elements, see eq. (14). This is because the determinant of the Jacobian \mathbf{J} , $\det|\mathbf{J}|$, is often non-constant for quadrilateral mapping, that is, $\det|\mathbf{J}|$ is

the following bilinear mapping is often employed to map the square domain in natural ξ - η coordinates into the quadrilateral domain in global x - y coordinates.

$$\mathbf{P}(x, y) = \sum_{i=1}^4 \mathbf{P}_i N_i(\xi, \eta), \quad (10)$$

where $\mathbf{P}(x, y)$ denotes the point in global coordinates; $\mathbf{P}_i = (x_i, y_i)$ are the global coordinates of four vertices; N_i are the bilinear functions and have the forms as

$$\begin{aligned} N_1 &= (1 - \xi)(1 - \eta), & N_2 &= \xi(1 - \eta), \\ N_3 &= \xi\eta, & N_4 &= (1 - \xi)\eta. \end{aligned} \quad (11)$$

The mapping Jacobian matrix is

$$\begin{aligned} \mathbf{J} &= \begin{bmatrix} J_{11} & J_{12} \\ J_{21} & J_{22} \end{bmatrix} = \begin{bmatrix} \partial x / \partial \xi & \partial y / \partial \xi \\ \partial x / \partial \eta & \partial y / \partial \eta \end{bmatrix} = \begin{bmatrix} (x_1 - x_2 + x_3 - x_4)\eta - x_1 + x_2 \\ (x_1 - x_2 + x_3 - x_4)\xi - x_1 + x_4 \end{bmatrix} \\ &= \begin{bmatrix} (y_1 - y_2 + y_3 - y_4)\eta - y_1 + y_2 \\ (y_1 - y_2 + y_3 - y_4)\xi - y_1 + y_4 \end{bmatrix}, \end{aligned} \quad (12)$$

a function of ξ and η , see eq. (12). In this situation, according to eqs. (13) and (14), \tilde{w}_x, \tilde{w}_y and consequently, \tilde{w}_n are rational functions of s that generally cannot be interpolated by nodal variables, resulting in the violation of the C^1 conformity. This is the reason why the C^1 conformity of Watkins's 5th-order elements is satisfied only for rectangular or parallelogram cases. In addition, because of the use of incomplete second-order derivatives as nodal variables [35], the BFS elements are valid only for rectangular elements with edges that parallel to the global axes.

3.2 C^1 conforming quadrilateral elements with 24 and 28 DOFs

Through the above discussion, one can find that a natural way to construct a C^1 conforming quadrilateral elements is to find \tilde{w} with both boundary deflections and normal derivatives in the forms of polynomials that can be uniquely determined by the nodal variables. This goal is achieved in this work by using the Hermite blending function interpolation presented in Sect 2. The main difference from those elements

by Watkins is on the construction of boundary functions, i.e. f_i and g_i in eqs. (1) and (8). In the following, the function \tilde{w} for our CQ24 elements, i.e. C^1 conforming quadrilateral element with 24 DOFs, is constructed to show the three steps of the present method.

Step 1. Define the boundary deflections and normal derivatives in global coordinates by the nodal variables.

As shown in Figure 3, each vertex of the CQ24 elements is assigned 6 DOFs, i.e. $w, w_x, w_y, w_{xx}, w_{yy}, w_{xy}$, defined in global coordinates; $\tau_i, \mathbf{n}_i, i=1, 2, 3, 4$, are the unit tangent and normal vectors on edge i ; v_i denotes vertex i ; s_i is the length coordinate of edge i . The original points for s_1 and s_3 are respectively v_1 and v_4 , and they are v_2 and v_1 for s_2 and s_4 .

Then for each edge i , the boundary deflection function w^{Ei} can be expressed in terms of the 5th-order Hermite interpolation and the nodal variables. For example, the boundary deflection w^{E1} on edge 1 can be interpolated by

$$\begin{aligned} w^{E1}(s_1) &= w^{v1}H_1(s_1) + w_{s_1}^{v1}H_2(s_1) + w_{s_1s_1}^{v1}H_3(s_1) \\ &\quad + w^{v2}H_4(s_1) + w_{s_1}^{v2}H_5(s_1) + w_{s_1s_1}^{v2}H_6(s_1), \\ s_1 &\in [0, L_1], \end{aligned} \quad (15)$$

where L_1 is the length of edge 1; $H_j(s_1), j=1-6$, are the 5th-order Hermite polynomials defined at interval $[0, L_1]$:

$$\begin{aligned} H_1(s_1) &= (L_1 - s_1)^3(L_1^2 + 3L_1s_1 + 6s_1^2)/L_1^5, \\ H_2(s_1) &= s_1(L_1 - s_1)^3(L + 3s_1)/L_1^4, \\ H_3(s_1) &= s_1^2(L_1 - s_1)^3/(2L_1^3), \\ H_4(s_1) &= s_1^3(10L_1^2 - 15L_1s_1 + 6s_1^2)/L_1^5, \\ H_5(s_1) &= -s_1^3(4L_1^2 - 7L_1s_1 + 3s_1^2)/L_1^4, \\ H_6(s_1) &= s_1^3(L_1 - s_1)^2/(2L_1^3). \end{aligned} \quad (16)$$

The coefficients w^{v1}, w^{v2} in eq. (15) are the nodal deflection at v_1 and v_2 , and $w_{s_1}^{v1}, w_{s_1s_1}^{v1}$ are the first and second-order derivatives of w with respect to s_1 on vertex 1, which can be expressed by the other nodal variables as

$$\begin{aligned} w_{s_1}^{v1} &= \frac{dw^{E1}(0)}{ds_1} = w_x^{v1}\tau_{1x} + w_y^{v1}\tau_{1y}, \\ w_{s_1s_1}^{v1} &= \frac{d^2w^{E1}(0)}{ds_1^2} = w_{xx}^{v1}\tau_{1x}^2 + w_{yy}^{v1}\tau_{1y}^2 + 2w_{xy}^{v1}\tau_{1x}\tau_{1y}, \end{aligned} \quad (17)$$

where $w_x^{v1}, w_y^{v1}, w_{xx}^{v1}, w_{yy}^{v1}, w_{xy}^{v1}$ are the nodal variables on vertex 1; τ_{1x}, τ_{1y} are the components of tangent vector τ_1 . The coefficients $w_{s_1}^{v2}, w_{s_1s_1}^{v2}$ on vertex 2 are defined similarly. Therefore, all the coefficients in eq. (15) are determined by the nodal variables at vertices 1 and 2. Similarly, $w^{E2}(s_2)$, $w^{E3}(s_3)$, $w^{E4}(s_4)$, can be constructed. Note that w^{Ei} for a given edge i is uniquely determined by the nodal variables at its two ends since the Hermite bases in eq. (16) are consistent with the collocation of the nodal variables. Therefore, the deflection function on a common edge of two adjacent ele-

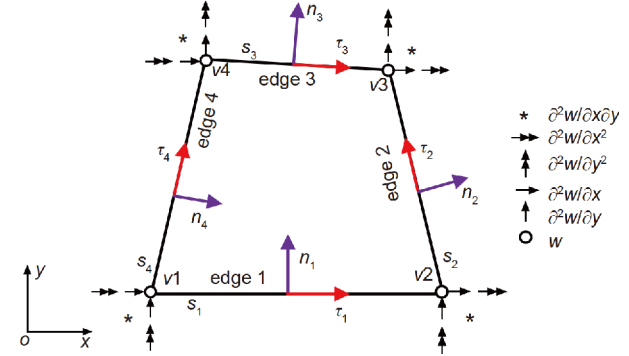


Figure 3 (Color online) DOFs collocation of CQ24 elements.

ments must be the same since they both are determined by the same nodal variables and the same Hermite bases. As a result, the C^0 continuity is first achieved.

Similarly, the boundary normal derivatives w_n^{Ei} can be defined. However, as the nodal variables are only sufficient to determine the first-order derivative of w_n^{Ei} with respect to s_i , the 3rd-order Hermite interpolation is hence used. For example, the normal derivative on edge 1 is interpolated as

$$\begin{aligned} w_n^{E1}(s_1) &= w_{n1}^{v1}h_1(s_1) + w_{n1s_1}^{v1}h_2(s_1) + w_{n1s_1s_1}^{v1}h_3(s_1) \\ &\quad + w_{n1s_1}^{v2}h_4(s_1), \end{aligned} \quad (18)$$

where $h_i, i=1, 2, 3, 4$, are the 3rd-order Hermite bases on $[0, L_1]$:

$$\begin{aligned} h_1(s_1) &= (L_1 - s_1)^2(L_1 + 2s_1)/L_1^3, \\ h_3(s_1) &= s_1^2(3L_1 - 2s_1)/L_1^3, \\ h_2(s_1) &= s_1(L_1 - s_1)^2/L_1^2, \\ h_4(s_1) &= s_1^2(s_1 - L_1)/L_1^2. \end{aligned} \quad (19)$$

The coefficient w_{n1}^{v1} in eq. (18) is the function value of w_n^{E1} on vertex 1; $w_{n1s_1}^{v1}$ is the first-order derivative of w_n^{E1} with respect to s_1 , and so forth. They can also be expressed in terms of the nodal variables $w_x^{v1}, w_y^{v1}, w_{xx}^{v1}, w_{yy}^{v1}, w_{xy}^{v1}$ on v_1 by

$$\begin{aligned} w_{n1}^{v1} &= w_n^{E1}(0) = n_{1x}w_x^{v1} + n_{1y}w_y^{v1}, \\ w_{n1s_1}^{v1} &= \frac{dw_n^{E1}(0)}{ds_1} \\ &= (w_{xx}^{v1}\tau_{1x} + w_{xy}^{v1}\tau_{1y})n_{1x} + (w_{xy}^{v1}\tau_{1x} + w_{yy}^{v1}\tau_{1y})n_{1y}, \end{aligned} \quad (20)$$

where n_{1x}, n_{1y} are the components of normal vector \mathbf{n}_1 . Likewise, $w_{n1}^{v2}, w_{n1s_1}^{v2}$ in eq. (18) can be expressed by the nodal variables at vertex 2. In the same way, the normal derivatives on the other three edges, i.e. $w_n^{E2}(s_2)$, $w_n^{E3}(s_3)$, $w_n^{E4}(s_4)$, can be determined. Thus it follows that the first-order normal derivative on the common edge of two adjacent elements are the same, and finally the C^1 conformity is achieved.

Step 2. Obtain the boundary functions f_i and g_i in eq. (9) in natural coordinates using the boundary deflections and nor-

mal derivatives obtained in Step 1.

After achieving the boundary deflections w_n^{Ei} and normal derivatives w_n^{Ei} , the remaining work is to achieve the element displacement function $\tilde{w}(x, y)$ which has the above specified boundary functions w^{Ei} and w_n^{Ei} . To this end, we firstly define $\tilde{w}(\xi, \eta)$ in natural coordinates by the blending function interpolation in eq. (8), then $\tilde{w}(x, y)$ can be obtained through the bilinear mapping in eq. (10). As stated in Sect 2, to determine $\tilde{w}(\xi, \eta)$ is to determine the boundary functions f_i and g_i , see eq. (8). Since the boundary deflections and normal derivatives of $\tilde{w}(x, y)$, i.e. w^{Ei} and w_n^{Ei} , should be matched, the functions f_i and g_i should be determined in accordance to w^{Ei} and w_n^{Ei} (note that in ref. [18] f_i and g_i are directly interpolated on the boundary of the rectangular domain in global coordinates). Therefore, f_i should be expressed as

$$\begin{aligned} f_1(\xi) &= w^{E1}(s_1), \quad s_1 = L_1\xi, \\ f_2(\eta) &= w^{E2}(s_2), \quad s_2 = L_2\eta, \\ f_3(\xi) &= w^{E3}(s_3), \quad s_3 = L_3\xi, \\ f_4(\eta) &= w^{E4}(s_4), \quad s_4 = L_4\eta, \end{aligned} \quad (21)$$

where L_i is the length of edge i . For the determination of g_i , the following chain rule is required:

$$\begin{bmatrix} \frac{\partial w}{\partial \xi} \\ \frac{\partial w}{\partial \eta} \end{bmatrix} = \begin{bmatrix} J_{11} & J_{12} \\ J_{21} & J_{22} \end{bmatrix} \begin{bmatrix} \frac{\partial w}{\partial x} \\ \frac{\partial w}{\partial y} \end{bmatrix}. \quad (22)$$

Using eq. (22) to each edge of the square domain as shown Figure 2(a) yields g_i as follows:

$$\begin{aligned} g_1(\xi) &= J_{21}(\xi)w_x^{E1} + J_{22}(\xi)w_y^{E1}, \\ g_2(\eta) &= J_{11}(\eta)w_x^{E2} + J_{12}(\eta)w_y^{E2}, \\ g_3(\xi) &= J_{21}(\xi)w_x^{E3} + J_{22}(\xi)w_y^{E3}, \\ g_4(\eta) &= J_{11}(\eta)w_x^{E4} + J_{12}(\eta)w_y^{E4}, \end{aligned} \quad (23)$$

where

$$\begin{aligned} w_x^{Ei} &= \frac{dw^{Ei}(s_i)}{ds_i} \tau_{ix} + w_n^{Ei}(s_i) n_{ix}, \\ w_y^{Ei} &= \frac{dw^{Ei}(s_i)}{ds_i} \tau_{iy} + w_n^{Ei}(s_i) n_{iy}, \\ i &= 1, 2, 3, 4. \end{aligned} \quad (24)$$

Step 3. Obtain the approximation field variable through blending function interpolation.

As stated in Step 2, substituting eqs. (21) and (23) into eq. (8) generates the element displacement function $\tilde{w}(\xi, \eta)$ which has the specified polynomial boundary deflections w^{Ei} and normal derivatives w_n^{Ei} . Note that the form of \tilde{w} is the same as the conventional finite elements where the field variable is a linear sum of shape functions, that is

$$\begin{aligned} \tilde{w}(\xi, \eta) = \sum_{i=1}^4 & \left(w^{v1} S_w^{v1} + w_x^{v1} S_{wx}^{v1} + w_y^{v1} S_{wy}^{v1} \right. \\ & \left. + w_{xx}^{v1} S_{wx}^{v1} + w_{xy}^{v1} S_{wy}^{v1} + w_{yy}^{v1} S_{wy}^{v1} \right), \end{aligned} \quad (25)$$

where S represents the nodal shape functions. For example, S_w^{v1} is the shape function of vertex 1 and is attached to the nodal deflection w^{v1} . In fact, if we let w^{v1} be 1 and all other remaining nodal variables be zero, the corresponding field variable \tilde{w} obtained by eq. (8) is exactly the shape function S_w^{v1} . And all other shape functions can be achieved in the same way.

From the above three steps, we can see that the shape functions depend on the element shape (because of the introduction of Jacobian in eq. (23)) and that is the key point why the present elements can keep C^1 continuity for arbitrarily quadrilateral elements. As a result, the expressions of the shape functions may vary from element to element, thus they are not presented here in an explicit form. Figure 4 shows some of the shape functions for vertex 1 and their derivatives, where S_{wx}^{v1} and S_{wx}^{v1} are attached to the first and second-order derivatives at vertex 1. One can observe the collocation properties of these shape functions. Similarly, we can develop the 28-DOFs conforming quadrilateral elements (CQ28) where 4th-order Hermite interpolation should be used for the determination of boundary normal derivatives, see eq. (18). The DOFs collocation of CQ28 is shown in Figure 5.

3.3 Checking the C^1 conformity of CQ24 and CQ28 elements

A numerical example shown in Figure 6 is used to check the C^1 conformity of the present elements. The square domain $[0, 1] \times [0, 1]$ is discretized by 4 arbitrarily shaped CQ24 and CQ28 elements. In the CQ24 model as shown in Figure 6(a), the DOFs at interior node 9 are arbitrarily specified as $[w, w_x, w_y, w_{xx}, w_{yy}, w_{xy}] = [1, 0.5, 1, 1.5, 2, 2.5]$, while the DOFs at other nodes are set as zeroes. It follows from Figure 7 that both the displacement field and its two first-order derivatives (calculated through eq. (14)) are continuous at the interfaces of elements, implying that the C^1 continuity of the CQ24 element is satisfied. The results for the CQ28 elements are presented in Figure 8, where the DOFs at node 9 have the same values as those of the CQ24 model, while the first-order normal derivatives at node 18, 19, 20, 21 are set to be 1, 2, 3, 4, respectively. One can see that the C^1 conformity is also achieved. Moreover, we note that for rectangular shapes, the present elements are exactly the same as Watkins's conforming elements [18].

3.4 Completeness of CQ24 and CQ28 elements

As well known, an effective C^1 element should be able to

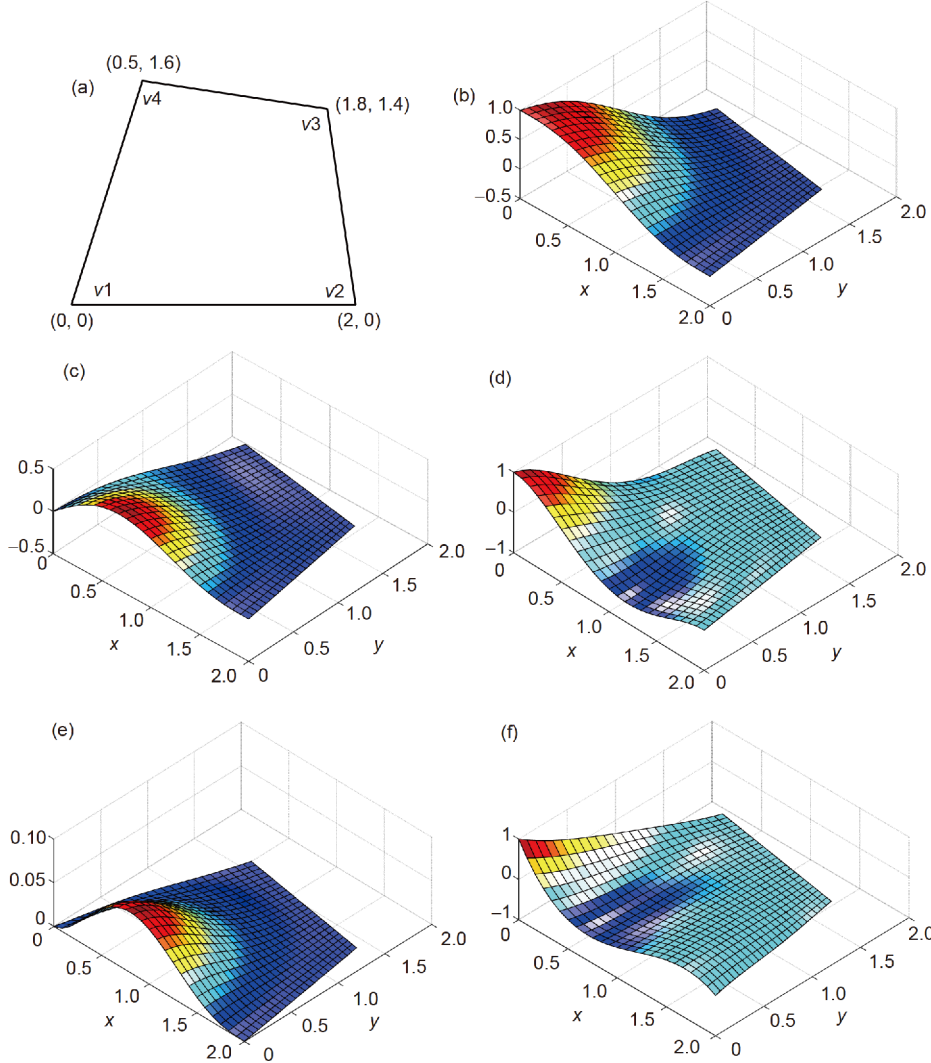


Figure 4 (Color online) Shape functions and its derivatives. (a) Element shape; (b) S_w^{v1} ; (c) $S_{w_x}^{v1}$; (d) $\partial S_{w_x}^{v1}/\partial x$; (e) $S_{w_{xx}}^{v1}$; (f) $\partial^2 S_{w_{xx}}^{v1}/\partial x^2$.

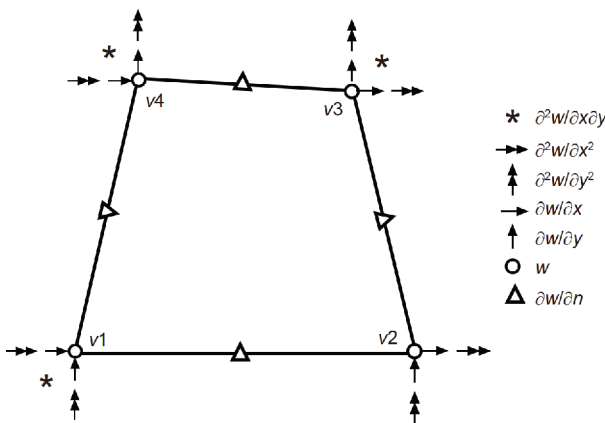


Figure 5 DOFs collocation of CQ28 elements.

reproduce the constant strain state, which means that the present elements should be sufficiently complete to reproduce the displacement field of $w=a_0+a_1x+a_2y+a_3x^2+a_4xy$

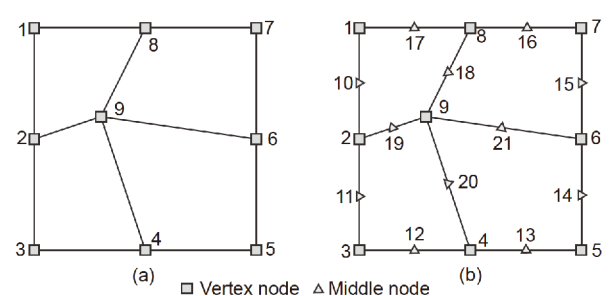


Figure 6 Meshes on square domains. (a) CQ24 elements; (b) CQ28 elements.

$+a_5y^2$. To check the completeness of the present elements, a commonly used patch test [12,23] is employed. The mesh and dimensions of the plate are shown in Figure 9(a), where the boundary deflection is prescribed by $w(x, y)=(1+x+2y+x^2+xy+y^2)/2$. Table 1 shows that both the CQ24 and CQ28 elements pass the patch test, indicating the present elements

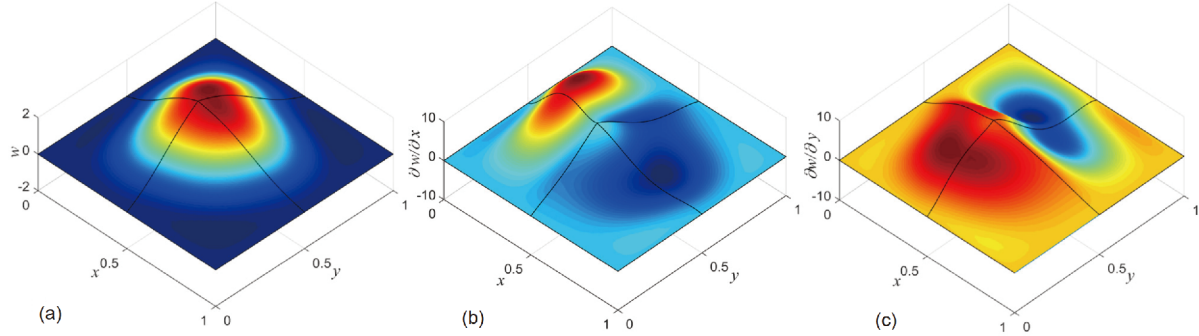


Figure 7 (Color online) C^1 conformity of CQ24 elements. (a) Continuity of displacement \tilde{w} ; (b) continuity of $\partial\tilde{w}/\partial x$; (c) continuity of $\partial\tilde{w}/\partial y$.

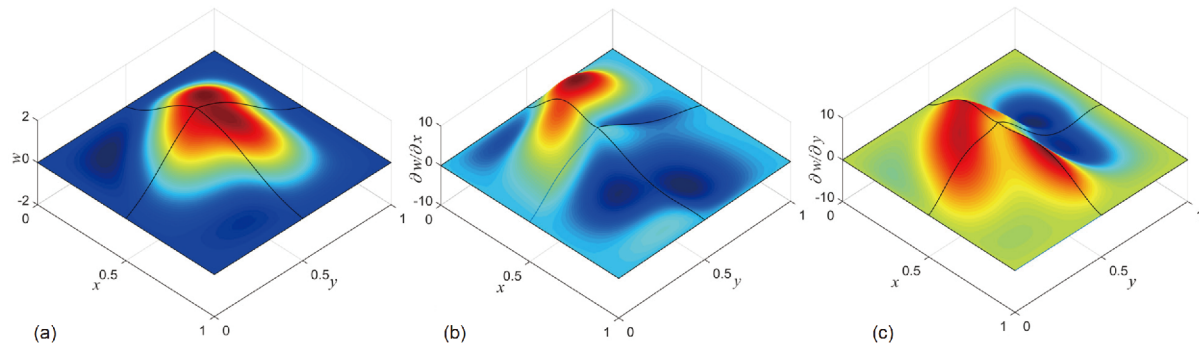


Figure 8 (Color online) C^1 conformity of CQ28 elements. (a) Continuity of displacement \tilde{w} ; (b) continuity of $\partial\tilde{w}/\partial x$; (c) continuity of $\partial\tilde{w}/\partial y$.

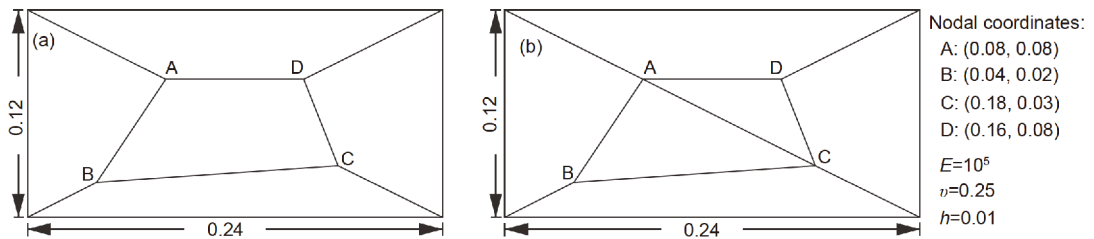


Figure 9 Meshes for patch test. (a) Quadrilateral elements only; (b) quadrilateral elements and triangular elements.

Table 1 Patch test for quadrilateral elements

Elements	Displacements			Moments		
	w	w_x	w_y	M_x	M_y	M_{xy}
CQ24	0.54140	0.55000	1.04000	0.01111	0.01111	0.00333
CQ28	0.54140	0.55000	1.04000	0.01111	0.01111	0.00333
Exact	0.54140	0.55000	1.04000	0.01111	0.01111	0.00333

complete at least to the second order. Moreover, in order to show the present elements can be used in cooperation with the triangular TUBA18 (TUBA elements with 18 DOFs) and TUBA21 (TUBA elements with 21 DOFs) elements, another patch test is performed with the mesh as shown in Figure 9(b). Table 2 shows that the patch test is also satisfied, showing these elements can work together in FEM simulation.

Moreover, by using projection test [16] we found that the polynomial spaces of the present elements vary with the element shape. As shown in Table 3, the complete orders of the rectangular CQ24 and CQ28 elements are respectively 4th and 5th order; for general quadrilateral shapes, the complete order of both elements reduced to 3rd order. Note that the omitted terms in Table 3, denoted by “...”, associate with the element shape, which means it is impossible to

Table 2 Patch test for the case of using quadrilateral elements and triangular elements together

Elements	Displacements			Moments		
	w	w_x	w_y	M_x	M_y	M_{xy}
CQ24 & TUBA18	0.54140	0.55000	1.04000	0.01111	0.01111	0.00333
CQ28 & TUBA21	0.54140	0.55000	1.04000	0.01111	0.01111	0.00333
Exact	0.54140	0.55000	1.04000	0.01111	0.01111	0.00333

Table 3 Polynomial spaces of CQ24 and CQ28 elements

Elements	Shape	Space
CQ24	Rectangular	Span [1, $x, y, x^2, xy, y^2, x^3, x^2y, xy^2, y^3, x^4, x^3y, x^2y^2, xy^3, y^4, x^5, x^3y^2, x^2y^3, y^5, \dots$] ^{a)}
	Quadrilateral	Span [1, $x, y, x^2, xy, y^2, x^3, x^2y, xy^2, y^3, \dots$]
CQ28	Rectangular	Span [1, $x, y, x^2, xy, y^2, x^3, x^2y, xy^2, y^3, x^4, x^3y, x^2y^2, xy^3, y^4, x^5, x^4y, x^3y^2, x^2y^3, x^2y^4, y^5, \dots$]
	Quadrilateral	Span [1, $x, y, x^2, xy, y^2, x^3, x^2y, xy^2, y^3, \dots$]

a) “...” denotes the incomplete terms in rectangular cases and the variational terms in quadrilateral cases.

construct these conforming quadrilateral elements through a fixed polynomial space.

3.5 Computational costs

As for efficiency, the computation cost of rectangular elements is less than that of quadrilateral elements because the element matrices of different rectangular elements are proportional to each other. For the CQ24 and CQ28 elements, the element matrices have to be calculated separately because of the inherent variety of element shape. Even though the formulation of the blending function interpolation in eq. (9) seems cumbersome, however, as the 3rd-order Hermite function h_i can be calculated once for all, only the boundary functions, i.e. f_i and g_i in eqs. (21) and (23), have to be calculated per element.

Compared with the isoparametric-like C^1 elements [12,36], matrix for DOFs transition is no longer required since the shape functions of the present elements are derived straightforwardly through the interpolation of nodal variables defined in global x - y coordinates. This benefits the improvement of computational efficiency. Beside, as it is shown in Sect. 5, the computation costs of the present ele-

ments can be justified by their high convergence rate. And they are also simpler than the subdivided quadrilateral elements [10,11] in computer programming.

4 Boundary conditions imposing and material discontinuity

In Sect. 5, the Kirchhoff plate problems are investigated using the present elements. The boundary-condition imposition for polygon domains have been discussed by many researchers [20,28], while in this section we discuss the more general curved cases, including the polygonal case as its special case. Note that the boundary conditions can be directly imposed at the middle nodes of CQ28 elements, so only vertex DOFs are discussed in the following.

Figure 10 shows a few cases of boundary conditions for the vertex node denoted by “v”. For cases (a) and (b) (Figure 10(a) and (b)), the boundary conditions are respectively C-C (two clamped boundaries) and C-S (one clamped and one simply supported boundary). In these cases, the boundary conditions can be imposed simply by letting all of the vertex DOFs be zeroes, i.e.,

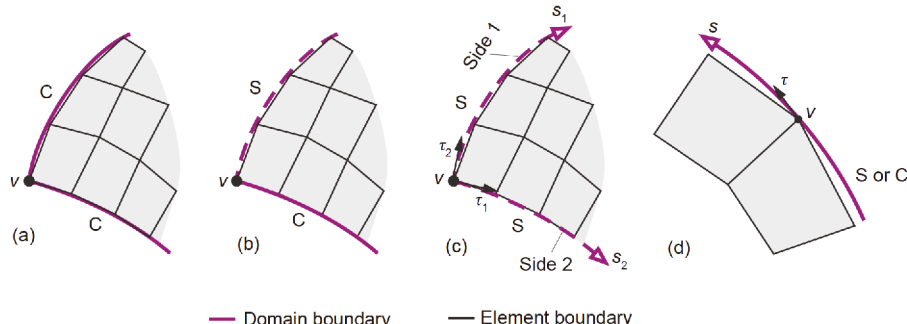


Figure 10 (Color online) Boundary conditions. (a) Two clamped edges; (b) one clamped edge and one simply supported edge; (c) two simply supported edges; (d) one clamped or simply supported edge.

$$\mathbf{w}_v = [w, w_x, w_y, w_{xx}, w_{yy}, w_{xy}]^T = \mathbf{0}. \quad (26)$$

In case (c) (Figure 10(c)), the domain is bounded by two simply supported edges. Let $x(s_i), y(s_i)$ denote the parameterizations of the domain boundary, i.e. side i ; s_i are the arc length coordinates for the boundary, and one should distinguish it from the length coordinates for element boundary. As the deflections on the two boundaries vanish, i.e. $w(s_i)=w(x(s_i), y(s_i))=0$, it follows:

$$w|_V = 0; \frac{dw}{ds_i}|_V = 0; \frac{d^2w}{ds_i^2}|_V = 0. \quad (27)$$

From $dw/ds_i=0$, $i=1, 2$, it follows:

$$\begin{aligned} \frac{dw}{ds_1} &= \frac{\partial w}{\partial x} \tau_{1x} + \frac{\partial w}{\partial y} \tau_{1y} = 0, \\ \frac{dw}{ds_2} &= \frac{\partial w}{\partial x} \tau_{2x} + \frac{\partial w}{\partial y} \tau_{2y} = 0, \end{aligned} \quad (28)$$

where $\tau_{1x}=dx/ds_1$, $\tau_{1y}=dy/ds_1$. They are components of the unit tangent vector $\boldsymbol{\tau}_1$, see Figure 10(c). Similarly, τ_{2x} and τ_{2y} are components of $\boldsymbol{\tau}_2$. We note that $\boldsymbol{\tau}_1$ and $\boldsymbol{\tau}_2$ are for the domain boundaries but for the element boundaries. One should also distinguish them from those in eq. (17). Since $\boldsymbol{\tau}_1$ and $\boldsymbol{\tau}_2$ are linearly independent, we can infer from eq. (28) that:

$$\frac{\partial w}{\partial x} = \frac{\partial w}{\partial y} = 0. \quad (29)$$

According to the chain rule, the third equation in eq. (27) is equivalent to

$$\begin{aligned} \frac{d^2w}{ds_i^2} &= \frac{\partial^2w}{\partial x^2} \left(\frac{dx}{ds_i} \right)^2 + 2 \frac{\partial^2w}{\partial x \partial y} \frac{dx}{ds_i} \frac{dy}{ds_i} + \frac{\partial^2w}{\partial y^2} \left(\frac{dy}{ds_i} \right)^2 \\ &\quad + \frac{\partial w}{\partial x} \frac{d^2x}{ds_i^2} + \frac{\partial w}{\partial y} \frac{d^2y}{ds_i^2} = 0. \end{aligned} \quad (30)$$

Substituting eq. (29) into eq. (30) yields:

$$\frac{d^2w}{ds_i^2} = \frac{\partial^2w}{\partial x^2} \tau_{ix}^2 + \frac{\partial^2w}{\partial x \partial y} 2\tau_{ix}\tau_{iy} + \frac{\partial^2w}{\partial y^2} \tau_{iy}^2 = 0. \quad (31)$$

From eqs. (29) and (31), the constraints in eq. (27) can be expressed in a matrix form as

$$\mathbf{T}_{ss} \mathbf{w}_v = \begin{bmatrix} 1 & & & & \\ & 1 & & & \\ & & 1 & & \\ & & & \tau_{1x}^2 & \tau_{1y}^2 & 2\tau_{1x}\tau_{1y} \\ & & & \tau_{2x}^2 & \tau_{2y}^2 & 2\tau_{2x}\tau_{2y} \\ \alpha_1 & \alpha_2 & \alpha_3 & & & \end{bmatrix} \begin{bmatrix} w \\ w_x \\ w_y \\ w_{xx} \\ w_{yy} \\ w_{xy} \end{bmatrix} = \begin{bmatrix} 0 \\ 0 \\ 0 \\ 0 \\ 0 \\ \lambda \end{bmatrix} = \mathbf{w}_v^{ss}, \quad (32)$$

where α_i ($i=1, 2, 3$) can be any values that make \mathbf{T}_{ss} nonsingular. A cross product of the fourth and fifth rows of \mathbf{T}_{ss} is recommended, i.e.,

$$[\alpha_1, \alpha_2, \alpha_3] = [\tau_{1x}^2, \tau_{1y}^2, 2\tau_{1x}\tau_{1y}] \times [\tau_{2x}^2, \tau_{2y}^2, 2\tau_{2x}\tau_{2y}]. \quad (33)$$

The variable λ in eq. (32) is a generalized nodal displacement to be solved. After the transformation in eq. (32), the vertex DOFs \mathbf{w}_v will be replaced by \mathbf{w}_v^{ss} , and the

boundary condition for case (c) can be imposed by letting the first five components of \mathbf{w}_v^{ss} be zeroes.

For case (d) (Figure 10(d)), the vertex locates on a curved domain boundary. The boundary could be simply supported or clamped. If the boundary is simply supported, it follows:

$$w|_V = 0; w_s = \frac{dw}{ds}|_V = 0; w_{ss} = \frac{d^2w}{ds^2}|_V = 0. \quad (34)$$

Using the similar analysis as above, they are simplified as

$$\mathbf{T}_s \mathbf{w}_v = \begin{bmatrix} 1 & & & & \\ & \tau_x & \tau_y & & \\ & \tau_x^* & \tau_y^* & \tau_x^2 & \tau_y^2 & 2\tau_x\tau_y \\ \alpha_1 & & \dots & & \alpha_5 & \\ \beta_1 & & \dots & & \beta_5 & \\ \gamma_1 & & \dots & & \gamma_5 & \end{bmatrix} \begin{bmatrix} w \\ w_x \\ w_y \\ w_{xx} \\ w_{yy} \\ w_{xy} \end{bmatrix} = \begin{bmatrix} 0 \\ 0 \\ 0 \\ \lambda_1 \\ \lambda_2 \\ \lambda_3 \end{bmatrix} = \mathbf{w}_v^s, \quad (35)$$

where $\alpha_i, \beta_i, \gamma_i$ ($i=1, 2, 3, 4, 5$) can be arbitrary values making \mathbf{T}_s nonsingular. A simple algorithm in Appendix is given for the calculation of them. And λ_1, λ_2 and λ_3 are the remaining three generalized nodal displacements; τ_x, τ_y are the Cartesian components of tangent vector $\boldsymbol{\tau}$; τ_x^* and τ_y^* are the curvature components defined by $\tau_x^*=d^2x/ds^2$, $\tau_y^*=d^2y/ds^2$, see also eq. (30). Then $\mathbf{w}_v^s = \mathbf{T}_s \mathbf{w}_v$ can be used as the new vertex DOFs, and the boundary condition is imposed by letting the first three components of \mathbf{w}_v^s be zeroes. Moreover, if the boundary is clamped, it follows:

$$\begin{aligned} w|_V &= 0; \frac{\partial w}{\partial x}|_V = 0; \frac{\partial w}{\partial y}|_V = 0; \frac{d^2w}{ds^2}|_V = 0; \\ \frac{d}{ds} \left(\frac{\partial w}{\partial x} \right)|_V &= 0; \frac{d}{ds} \left(\frac{\partial w}{\partial y} \right)|_V = 0. \end{aligned} \quad (36)$$

There are six constraints in eq. (36). However, only five of them are independent, and are simplified as

$$\mathbf{T}_c \mathbf{w}_v = \begin{bmatrix} 1 & & & & \\ & 1 & & & \\ & & 1 & & \\ & & & \tau_x & \tau_y \\ & & & \tau_y & \tau_x \\ \alpha_1 & \alpha_2 & \alpha_3 & & \end{bmatrix} \begin{bmatrix} w \\ w_x \\ w_y \\ w_{xx} \\ w_{yy} \\ w_{xy} \end{bmatrix} = \begin{bmatrix} 0 \\ 0 \\ 0 \\ 0 \\ 0 \\ \lambda \end{bmatrix} = \mathbf{w}_v^c, \quad (37)$$

where α_i ($i=1, 2, 3$) is determined by making \mathbf{T}_c nonsingular, and it can be obtained by the cross product of the 3rd and 4th rows of \mathbf{T}_c . And λ is the generalized nodal displacement. The boundary condition can be imposed by forcing the first 5 components of \mathbf{w}_v^c be zeroes.

For plate with material discontinuity (Figure 11), the strains are often discontinuous. As a result, the second order derivatives of the exact solution is discontinuous along the material boundary, which implies a rigorously C^1 conforming solution, i.e. only w, w_x and w_y are continuous. However, since the second order derivatives are used as the nodal variables in present elements, an over conforming solution

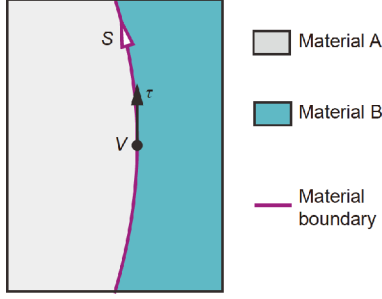


Figure 11 (Color online) Plate with material discontinuity.

space will be generated if we assemble the elements in the usual manner by sharing the common nodal variables. Finally, the solutions will not converge. To solve this problem, one may notice that the enforcement of the rigorously C^1 conformity on material boundary is equivalent to specifying the same nonhomogeneous clamped boundary condition along the material boundary for the elements belong to different material area. For the vertex shown in Figure 11, because the displacement w is continuous along the boundary, we can infer that w , w_s , w_{ss} are continuous along the boundary. As in eqs. (28) and (30), w_s and w_{ss} are expressed as

$$\begin{aligned} w_s &= \frac{dw(x(s), y(s))}{ds} = w_x \tau_x + w_y \tau_y, \\ w_{ss} &= \frac{d^2w(x(s), y(s))}{ds^2} \\ &= w_{xx} \tau_x^2 + w_{yy} \tau_y^2 + 2w_{xy} \tau_x \tau_y + w_x \tau_x^* + w_y \tau_y^*, \end{aligned} \quad (38)$$

where $x(s)$ and $y(s)$ denote the parameterization of boundary curve as in Figure 10. Similarly, because of the continuous of normal derivative, we have w_n and w_{ns} are continuous along the boundary. They are expressed by

$$\begin{aligned} w_n &= w_x \tau_y - w_y \tau_x, \\ w_{ns} &= \frac{dw_n}{ds} = w_x \tau_y^* - w_y \tau_x^* + w_{xx} \tau_x \tau_y \\ &\quad - w_{yy} \tau_x \tau_y + w_{xy} (\tau_y^2 - \tau_x^2). \end{aligned} \quad (39)$$

Note that the continuity of w_s and w_n is equivalent to the continuity of w_x and w_y . Then we can define a new vector \mathbf{w}_v^m as the transformed nodal variables through

$$\begin{aligned} \mathbf{w}_v^m &= \begin{bmatrix} w \\ w_x \\ w_x \\ w_{ss} \\ w_{ns} \\ \lambda \end{bmatrix} = \begin{bmatrix} 1 & & & & & \\ & 1 & & & & \\ & & 1 & & & \\ \tau_x^* & \tau_y^* & \tau_x^2 & \tau_y^2 & 2\tau_x \tau_y & \\ \tau_y^* & -\tau_x^* & \tau_x \tau_y & -\tau_x \tau_y & (\tau_y^2 - \tau_x^2) & \\ \alpha_1 & \alpha_2 & \alpha_3 & \alpha_4 & \alpha_5 & \end{bmatrix} \begin{bmatrix} w \\ w_x \\ w_y \\ w_{xx} \\ w_{yy} \\ w_{xy} \end{bmatrix} \\ &= \mathbf{T}_m \mathbf{w}_v, \end{aligned} \quad (40)$$

where \mathbf{T}_m is the transition matrix for material discontinuity; α_i can be easily determined by making \mathbf{T}_m nonsingular; λ is the generalized nodal variable. Consequently, the C^1 con-

formity can be imposed by sharing only the first five terms of \mathbf{w}_v^m on the common vertex of elements from different material areas. As for computation, the curved boundary is often expressed in a parametric form of parameter t rather than the arc length s , i.e. $x=x(t)$, $y=y(t)$. The components of tangent vector and their derivatives with respect to s in eqs. (32), (35), (37) and (40) can be calculated by the following equations:

$$\begin{aligned} \tau_x &= \frac{dx}{ds} = \frac{a}{\sqrt{a^2+b^2}}, \\ \tau_x^* &= \frac{d^2x}{ds^2} = \frac{c}{a^2+b^2} - a(a^2+b^2)^{-2}(ac+bd), \\ \tau_y &= \frac{dy}{ds} = \frac{b}{\sqrt{a^2+b^2}}, \\ \tau_y^* &= \frac{d^2y}{ds^2} = \frac{d}{a^2+b^2} - b(a^2+b^2)^{-2}(ac+bd), \\ a &= x'(t), b = y'(t), c = x''(t), d = y''(t). \end{aligned} \quad (41)$$

5 Numerical results

In this section, numerical examples are employed to assess the performance of the present CQ24 and CQ28 elements. Firstly, the bending problems of square and triangular plates are investigated to check the convergence of the CQ24 and CQ28 elements. Then vibration analysis of sectorial plates is used as the application of these two elements in problems with curvilinear-bounded domain. The problem of material discontinuity is considered in the last example. Since the combinational use with TUBA elements is trivial as shown in Sect. 3.4, numerical examples for this case are therefore not shown here. In all results, the present elements are compared with Fraeijs de Veubeke's quadrilateral elements [11] because they are all C^1 conforming.

5.1 Bending of square plate

Consider a fully simply supported square plate with domain $[0, a] \times [0, a]$, where a is the side length, under sinusoidal distributed load.

$$q = q_0 \sin\left(\frac{\pi x}{a}\right) \sin\left(\frac{\pi y}{a}\right), \quad (42)$$

where q_0 is the load factor. The exact solution [12] is given by

$$w^*(x, y) = \frac{q_0 a^4}{4\pi^4 D} \sin\left(\frac{\pi x}{a}\right) \sin\left(\frac{\pi y}{a}\right), \quad (43)$$

in which $D=Eh^3/12(1-v^2)$ is the flexural rigidity; E is the modulus; v the Poisson's ratio; h the thickness. The material and geometric constants are taken as $E=206$ GPa, $v=0.3$, $h=0.01$ m, and $a=1$ m, $q_0=-2$ kN/m². Regular (Reg.) and distorted (Dist.) meshes for convergence study are shown in

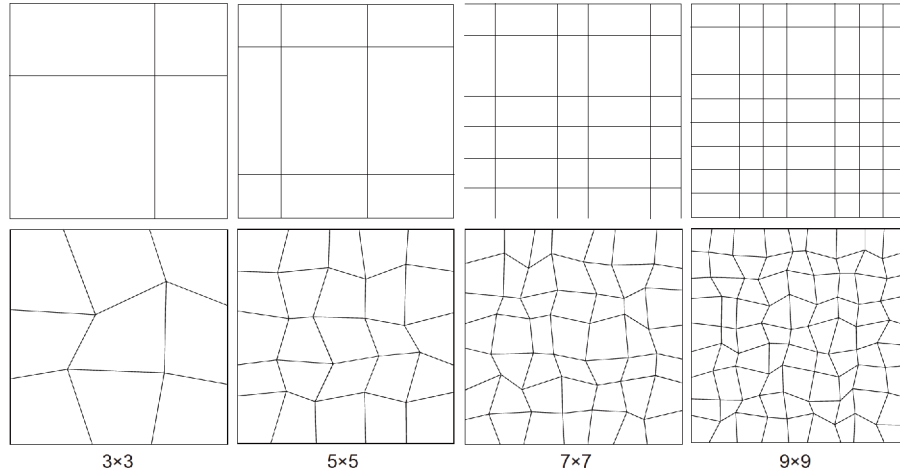


Figure 12 Regular and distorted meshes for square plates.

Figure 12.

Table 4 shows the numerical results of central-point deflection and bending moment M_x obtained by regular and distorted CQ28, CQ24 and Fraeijis de Veubeke's elements. The exact solutions are also contained for comparison. As it can be seen, the CQ24 and CQ28 elements are very accurate even when very coarse meshes like 3×3 mesh are used. All the results of the present elements converge very fast to the exact solutions, while the Fraeijis de Veubeke's elements are less accurate than the present elements when the same meshes are used. As expected, the deflection converges faster than the bending moment in all cases. **Figure 13** shows the absolute errors of bending moment obtained by using 9×9 distorted mesh. One can also see that the present conforming elements are much more accurate than Fraeijis de Veubeke's elements. Moreover, the CQ28 element is more accurate than the CQ24 element.

To assess the global convergence, we use the following

error in energy norm:

$$\|e\|_E = \left[D \iint_{\Omega} \left(\frac{\partial^2 e}{\partial x^2} \right)^2 + \left(\frac{\partial^2 e}{\partial y^2} \right)^2 + 2v \frac{\partial^2 e}{\partial x^2} \frac{\partial^2 e}{\partial y^2} + 2(1-v) \left(\frac{\partial^2 e}{\partial x \partial y} \right)^2 dx dy \right]^{1/2}, \quad (44)$$

where $e = w^* - w_{app}$ is the difference of numerical solution w_{app} and the exact solution w^* . As it can be seen from **Figure 14**, the present elements converge faster than Fraeijis de Veubeke's elements no matter for regular or distorted elements. For distorted meshes, the convergence rate of the CQ28 element decreases more evidently than the other two elements. This is because the decrease of the complete order in CQ28 element is more prominent as can be seen from **Table 3**. Nevertheless, the convergence rate of the CQ28 element is still higher than the other two elements.

Table 4 Central-point deflection and moment for the simply supported square plate under sinusoidal load

Method	Mesh				Exact
	3×3	5×5	7×7	9×9	
Central deflection ($\times 10^{-4}$)	Reg.CQ24	2.7203	2.7210	2.7210	2.7210
	Dist.CQ24	2.7202	2.7210	2.7210	2.7210
	Reg.CQ28	2.7210	2.7210	2.7210	2.7210
	Dist.CQ28	2.7209	2.7209	2.7210	2.7210
	Reg. Veubeke	2.7216	2.7210	2.7210	2.7210
Central bending moment M_x	Dist. Veubeke	2.7084	2.7207	2.7207	2.7208
	Reg.CQ24	65.5456	65.8160	65.8476	65.8546
	Dist.CQ24	65.5540	65.8168	65.8440	65.8489
	Reg.CQ28	65.8418	65.8566	65.8582	65.8586
	Dist.CQ28	65.8170	65.8620	65.8568	65.8558
Reg. Veubeke	71.3520	67.9555	66.9458	66.5207	65.8588
	Dist. Veubeke	64.4767	68.8392	66.2897	65.9333

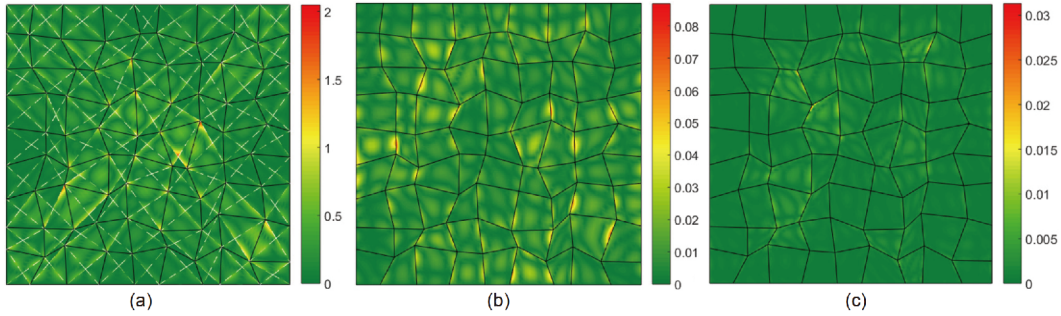


Figure 13 (Color online) Absolute errors of bending moment M_x using distorted quadrilateral mesh 9×9 . (a) Fraeij de Veubeke's elements; (b) CQ24; (c) CQ28.

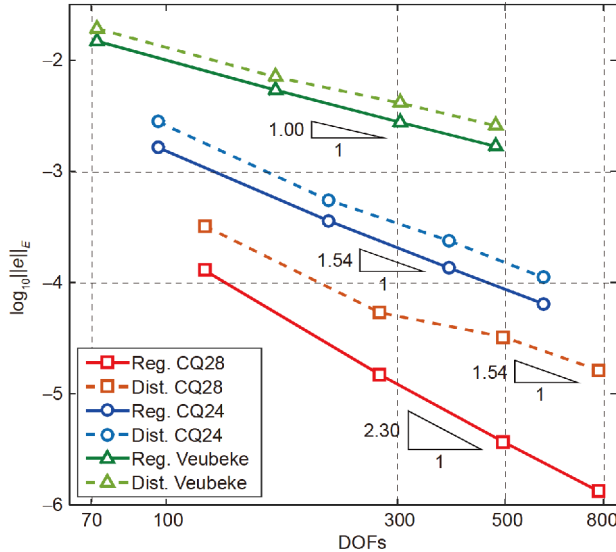


Figure 14 (Color online) Convergence of error in energy norm for square plate.

5.2 Bending of triangular plate

Here a simply supported equilateral triangular plate under uniform load q is considered. Figure 15 shows the dimensions as well as the coarsest and finest meshes. The normalized central deflection and bending moment are listed in Table 5 where the exact solutions [37] are also presented for comparison. As it can be observed that both deflection and bending moment obtained by the present two elements are in excellent agreement with the exact solutions when $3 \times 4 \times 4$

elements are used. Figure 16 shows the convergence of the error in energy norm. Fast convergence is again observable.

5.3 Plates with curved boundaries

In this example, the vibration of a sectorial plate is considered. The geometric dimensions and mesh are shown in Figure 17, where a is the inner radius, b is the outer radius, θ the circumferential angle. To improve accuracy, more elements are used along the circumferential direction. The boundary conditions of SSSS, SFSF and SCSC are considered. The SCSC boundary condition implies the two radial boundaries are simply supported, while the other two are clamped. Table 6 compares the first four non-dimensional frequencies with the exact solutions [38–40]. Good convergence of the present results is observed again. When the mesh is 5×10 , most results match well with reference solutions. The convergence of the first two normalized non-dimensional frequencies for SSSS and SCSC sectorial plates is presented in Figure 18 respectively. One can see that the convergence rate of the present elements is still higher than Fraeij de Veubeke's elements. Figure 19 plots the first four bending modes for 90° SSSS plate and 45° SCSC plate, respectively.

5.4 Plates with material discontinuity

The simply supported square plate with material discontinuity under uniform load $q = -2000 \text{ N/m}^2$ is employed as

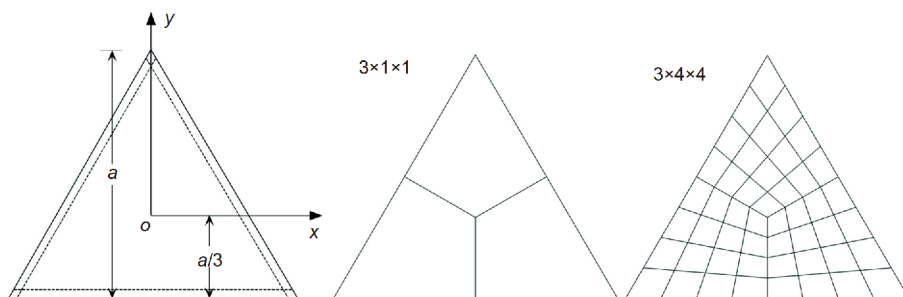
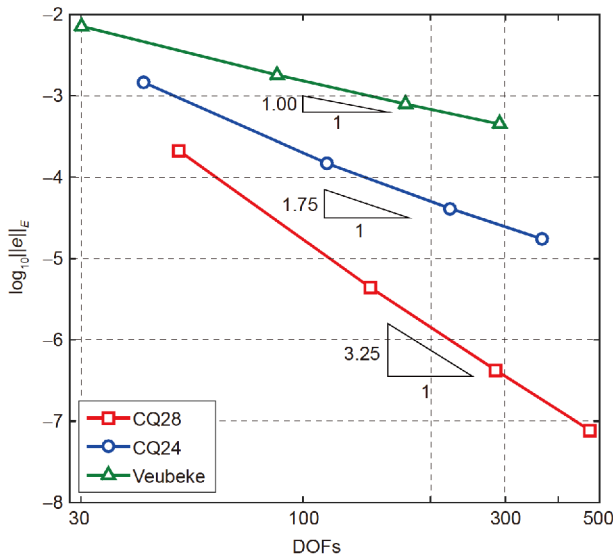
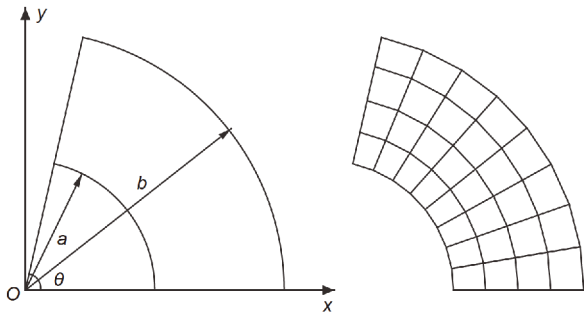


Figure 15 A simply supported equilateral plate and the meshes.

Table 5 Normalized central deflection and moment for the simply supported equilateral triangular plate under uniform load ($v=0.3$)

Method	Mesh				Exact
	$3 \times 1 \times 1$	$3 \times 2 \times 2$	$3 \times 3 \times 3$	$3 \times 4 \times 4$	
$wD/(qa^4) (\times 10^{-3})$	CQ24	1.02938	1.02876	1.02880	1.02881
	CQ28	1.02936	1.02880	1.02881	1.02881
	Veubeke	0.96451	1.02631	1.02838	1.02867
$M_x/(qa^2)$	CQ24	0.02189	0.02399	0.02406	0.02407
	CQ28	0.02453	0.02408	0.02407	0.02407
	Veubeke	0.03115	0.02532	0.02458	0.02435

**Figure 16** (Color online) Convergence of the error in energy norm for equilateral triangular plates.**Figure 17** A sectorial plate and the meshes (4×8).

our last example. As shown in Figure 20, the side length $a=1$ m, the thickness $h=0.01$ m. The materials are distinguished by different colors with $E_1=100$ GPa, $v_1=0.3$ for the yellow region and $E_2=200$ GPa, $v_2=0.25$ for the green region. Since the same DOFs are used at the vertices of our CQ28 and CQ24 elements, only CQ28 element is used in this example without loss of generality. Three types of material

boundaries, denoted by line or curve A-B, are considered as shown in Figure 20, where meshes are also presented for three cases. The approach of dealing with material discontinuities presented in Sect. 4 is used here. Since Fraeijs de Veubeke's elements are rigorously C^1 conforming elements as opposed to the over C^1 conforming elements with second-order-derivative continuity on vertices, solutions obtained by these elements are therefore used as the references for our elements. Figure 21 shows the meshes for Fraeijs de Veubeke's elements.

In the first case, as shown in Figure 20(a), the material boundary is a straight line that parallels to plate side. As a result, no singularity of the solution is caused by the material discontinuity. Rectangular elements are used for domain discretization. In Figure 22(a) and (b), we plot the normal bending moments obtained by CQ28 and Fraeijs de Veubeke's elements from two different material areas. Good agreement between them is observed. Figure 22(c) compares the normal bending moments obtained by our elements from different material regions. One can see that the results match well with each other, indicating that the continuity of the normal bending moment is satisfied well. In the second case as shown in Figure 20(b), the material boundary is a sloping line, so the quadrilateral elements are used to discretize the domain. Since moment singularity may arise at the two ends of line A-B, a graded mesh shown in Figure 21(b) is used for Fraeijs de Veubeke's elements to capture the singularity of bending moment (note that the singularity is caused by itself of plate theory not the finite element method). Figure 23(a) and (b) shows that the present results agree well with the solution by Fraeijs de Veubeke's element. From Figure 23(c), one can see that the continuity of the normal bending moment is satisfied well except the singular ends (note that the singularity exists also at the end $y=0$, though it is too small to be identified in this figure). In the third case as shown in Figure 20(c), the material boundary A-B is a parabolic curve. To capture geometric property, more CQ28 elements are used in this case. The results are shown in Figure 24. It follows that, due to the inherent geometry discretization er-

Table 6 First four frequency of sectorial plates

Mode	Mesh				Exact	
	2×4	3×6	4×8	5×10		
SSSS, $b/a=2.0$, $\theta=\pi/2$, $\Omega=\omega b^2 \sqrt{\rho h/D}$, CQ24	1	47.127	47.107	47.099	47.096	47.089
	2	68.309	68.350	68.364	68.370	68.379
	3	103.052	103.239	103.325	103.366	103.437
	4	151.403	150.535	150.720	150.813	150.982
SFSF, $b/a=2.0$, $\theta=\pi/2$, $\Omega=a(\omega\sqrt{\rho h/D})^{1/2}$, CQ24	1	1.0465	1.0392	1.0366	1.0354	1.0333
	2	2.3240	2.3079	2.3023	2.2996	2.2950
	2	2.8245	2.8048	2.7979	2.7947	2.7892
	4	3.4732	3.4494	3.4410	3.4371	3.4301
SSSS, $b/a=2.0$, $\theta=\pi/4$, $\Omega=\omega b^2 \sqrt{\rho h/D}$, CQ28	1	68.364	68.373	68.376	68.377	68.379
	2	150.72	150.86	150.92	150.94	150.98
	3	189.72	189.63	189.61	189.61	189.60
	4	277.84	278.09	278.22	278.28	278.39
SCSC, $b/a=2.0$, $\theta=\pi/4$, $\Omega=\omega b^2 \sqrt{\rho h/D}$, CQ28	1	108.36	107.89	107.74	107.67	107.57
	2	179.77	179.22	179.04	178.95	178.82
	3	272.49	270.36	269.94	269.76	269.49
	4	307.31	306.43	306.17	306.05	305.84

rors, the results are not as smooth as the first two cases. However, the present results still match well with the solutions by Fraeijs de Veubeke's elements. From Figure 24(c)

one can observe the good continuity of the normal bending moment except the two singular ends. All these results verified the effectiveness of the proposed method for dealing

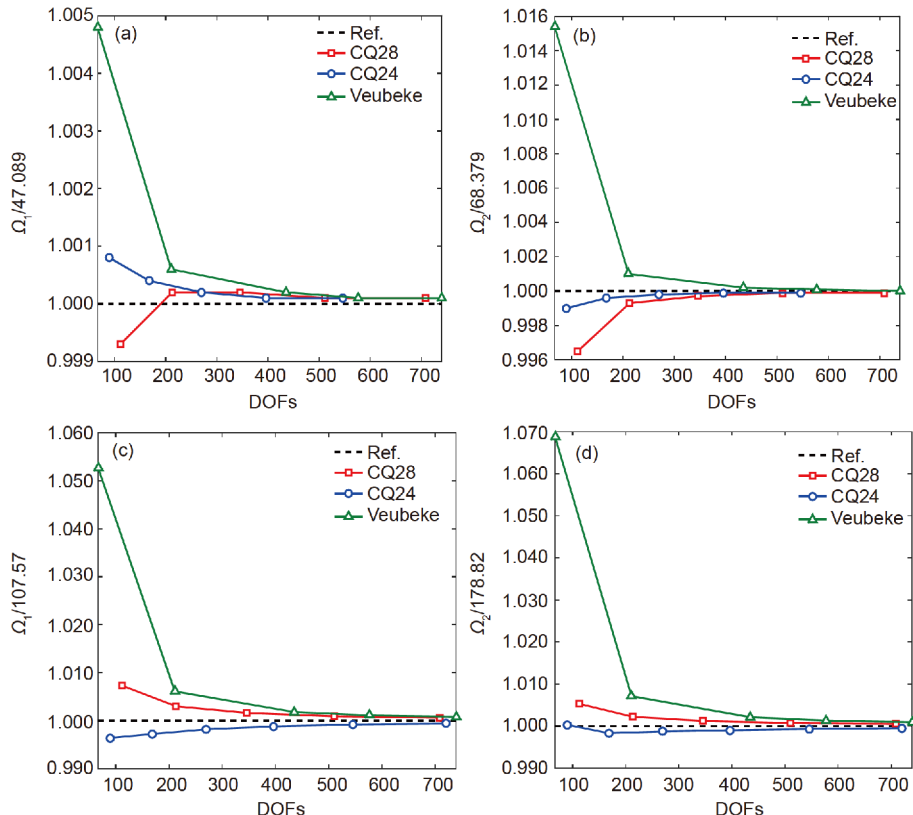


Figure 18 (Color online) Convergences of frequency parameters for the SSSS 90° (a), (b), and SCSC 45° (c), (d) sectorial plates. (a), (c) The first order; (b), (d) the second order.

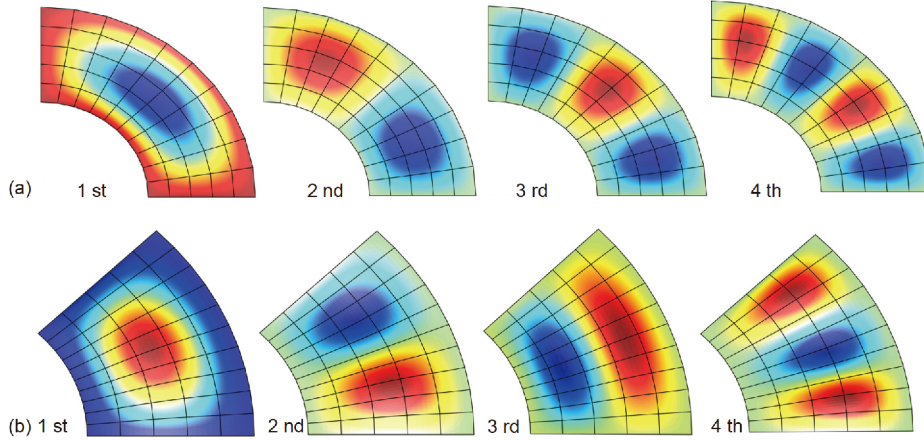


Figure 19 (Color online) The first four mode shapes of the SSSS 90° (a) and SCSC 45° (b) sectorial plates. (a) Obtained by CQ24 elements; (b) obtained by CQ28 elements.

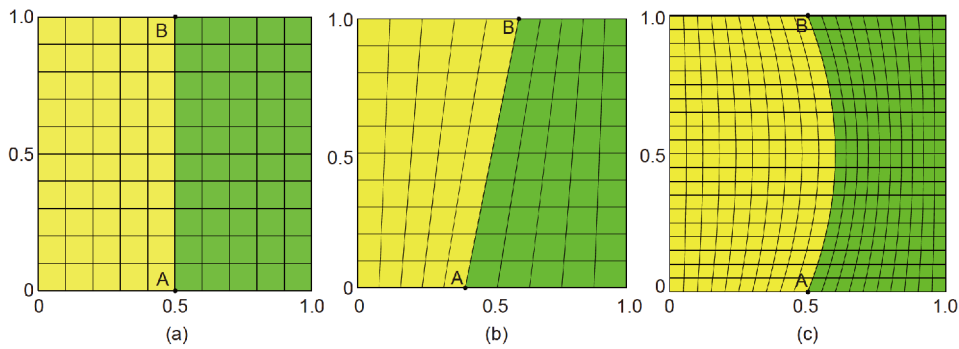


Figure 20 (Color online) CQ28 meshes for square plates with material discontinuity. (a) Material boundary parallels to axis y ; (b) sloping material boundary; (c) curved material boundary.

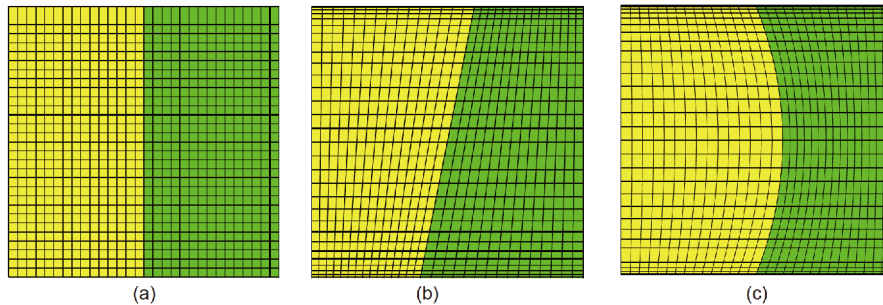


Figure 21 (Color online) Meshes for Fraeijs de Veubkeke's elements. (a) Material boundary parallels to axis y ; (b) sloping material boundary; (c) curved material boundary.

with the problem with material discontinuity.

6 Conclusion

The C^1 conforming quadrilateral elements with second-order derivatives at corner nodes were constructed in this work based on the blending function interpolation method. The

novelty of the present elements is that the geometric information of element is considered in the construction of shape functions. It was concluded that the present elements can keep C^1 conforming for arbitrarily shaped convex quadrilaterals. It was found that the solution spaces of elements vary with element shapes when satisfying the requirement of C^1 conformity, and the complete order of the present elements is at least third order and at most fifth order.

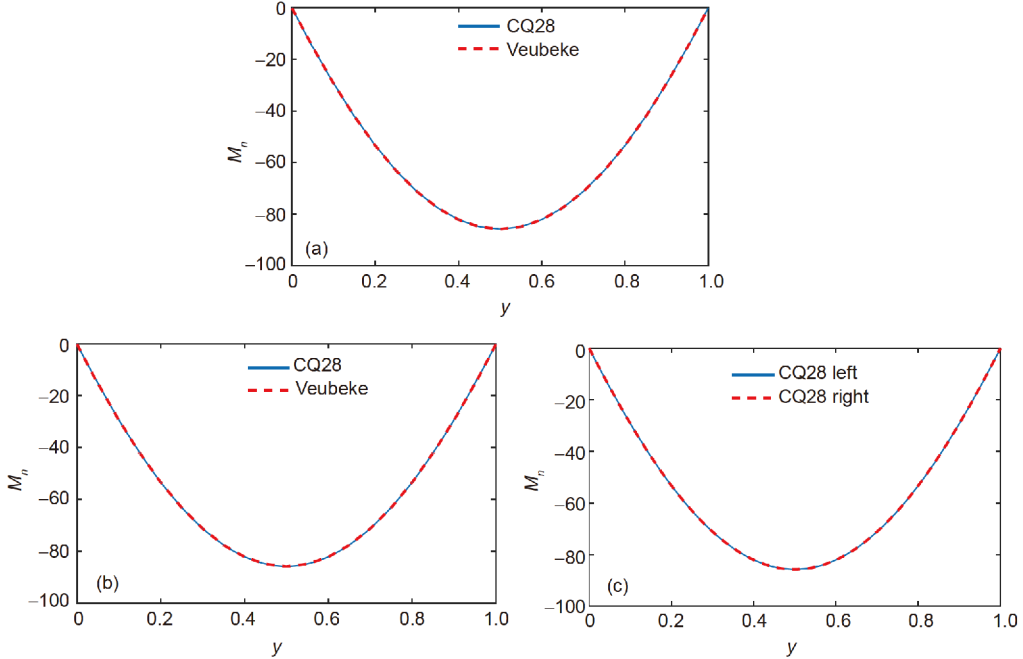


Figure 22 (Color online) Normal bending moment comparison along line A-B for case 1. (a) Moments on the left side of line A-B; (b) moments on the right side of line A-B; (c) moment comparison of left and right sides of line A-B.

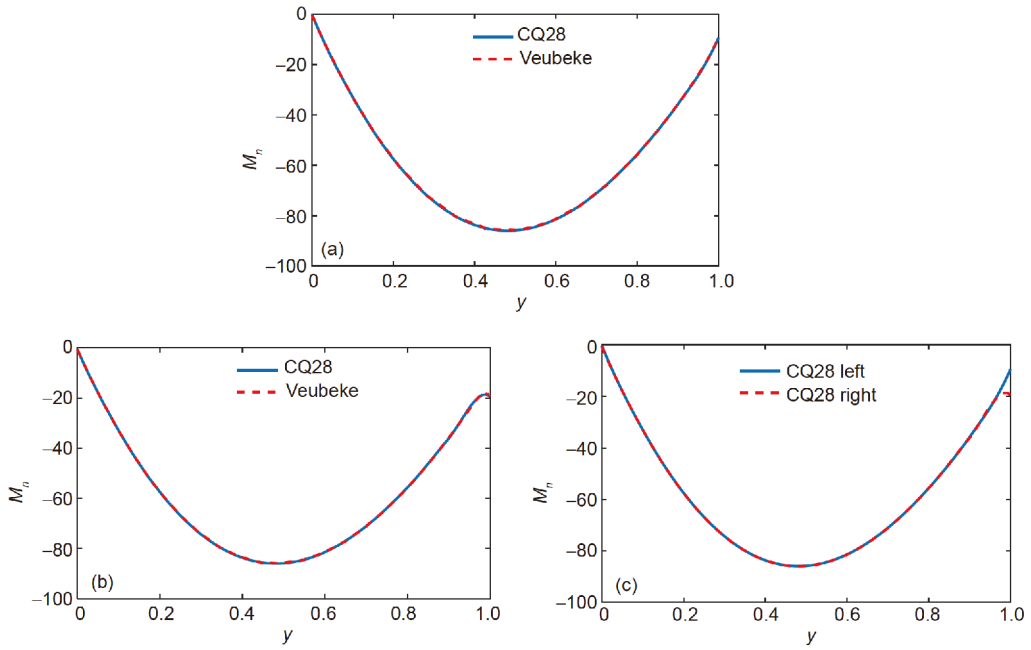


Figure 23 (Color online) Normal bending moment comparison along line A-B for case 2. (a) Moments on the left side of line A-B; (b) moments on the right side of line A-B; (c) moment comparison of left and right sides of line A-B.

Faster convergence was verified by numerical examples. In addition, we also proposed a simple method of nodal DOFs replacement to deal with the boundary-condition imposition and the material discontinuity on general curved boundaries. It is expected that the present elements should be a significant completeness of the family of high-precision C^1 conforming rectangular and triangular finite elements.

Appendix

An algorithm for the computation of vectors $\alpha=[\alpha_1, \dots, \alpha_5]$, $\beta=[\beta_1, \dots, \beta_5]$, $\gamma=[\gamma_1, \dots, \gamma_5]$, which are linearly independent with $[\tau_x, \tau_y, 0, 0, 0]$, $[\tau_x^*, \tau_y^*, \tau_x^2, \tau_y^2, 2\tau_x\tau_y]$.
if $\text{abs}(\tau_x) > 0$

$$\text{if } \text{abs}(\tau_y^*\tau_x - \tau_x^*\tau_y) > 0$$

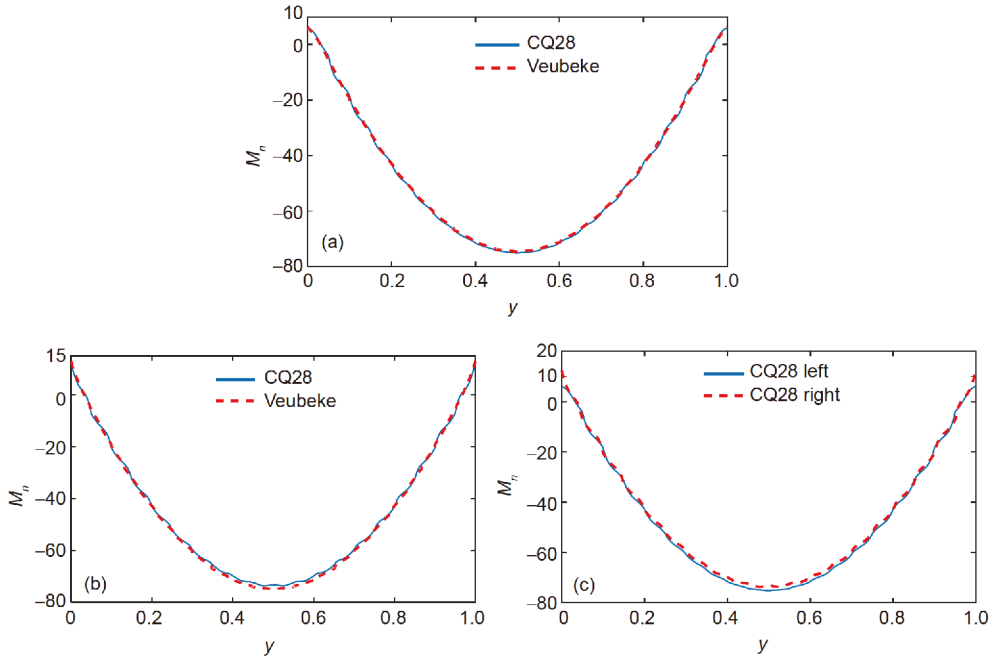


Figure 24 (Color online) Normal bending moment comparison along curve A-B for case 3. (a) Moment on the left side of curve A-B; (b) moments on the right side of curve A-B; (c) moment comparison of left and right sides of curve A-B.

```

 $\alpha=[0\ 0\ 1\ 0\ 0]$ ;  $\beta=[0\ 0\ 0\ 1\ 0]$ ;  $\gamma=[0\ 0\ 0\ 0\ 1]$ ;
else
   $\alpha=[0\ 1\ 0\ 0\ 0]$ ;  $\beta=[0\ 0\ 0\ 1\ 0]$ ;  $\gamma=[0\ 0\ 0\ 0\ 1]$ ;
end
else (% implies  $\tau_y \neq 0$  since  $\tau_x^2 + \tau_y^2 = 1$ )
  if abs( $\tau_y^*\tau_x - \tau_x^*\tau_y$ )>0
     $\alpha=[0\ 0\ 1\ 0\ 0]$ ;  $\beta=[0\ 0\ 0\ 1\ 0]$ ;  $\gamma=[0\ 0\ 0\ 0\ 1]$ ;
  else
     $\alpha=[1\ 0\ 0\ 0\ 0]$ ;  $\beta=[0\ 0\ 1\ 0\ 0]$ ;  $\gamma=[0\ 0\ 0\ 0\ 1]$ ;
  end
end

```

This work was supported by the National Natural Science Foundation of China (Grant Nos. 11402015, 11872090 & 11672019).

- 1 Cottrell J A, Hughes T J R, Reali A. Studies of refinement and continuity in isogeometric structural analysis. *Comput Method Appl Mech Eng*, 2007, 196: 4160–4183
- 2 Surana K S, Reddy J N, Allu S. The k-version of finite element method for initial value problems: Mathematical and computational framework. *Int J Comput Method Eng Sci Mech*, 2007, 8: 123–136
- 3 Surana K S, Petti S R, Ahmadi A R, et al. On p-version hierarchical interpolation functions for higher-order continuity finite element models. *Int J Comp Eng Sci*, 2012, 02: 653–673
- 4 Oñate E. Structural Analysis with the Finite Element Method. Volume 2. Linear Statics: Beams, Plates and Shells. Netherland: Springer, 2013. 438–524
- 5 Zhao J, Chen W J, Lo S H. A refined nonconforming quadrilateral element for couple stress/strain gradient elasticity. *Int J Numer Meth Eng*, 2011, 85: 269–288
- 6 Sap D. Conforming Stokes elements yielding divergence-free approximations on quadrilateral Meshes. Dissertation of Doctoral Degree. Pittsburgh: University of Pittsburgh, 2017
- 7 Clough R W, Tocher J L. Finite element stiffness matrices for analysis of plate bending. In: Proceedings of the Conference on Matrix Methods in Structural Mechanics: WPAFB. Ohio, 1965. 515–545
- 8 Argyris J H, Fried I, Scharpf D W. The TUBA family of plate elements for the matrix displacement method. *Aeronaut J*, 1968, 72: 701–709
- 9 Bell K. A refined triangular plate bending finite element. *Int J Numer Meth Eng*, 1969, 1: 101–122
- 10 Clough R W, Felippa C A. A refined quadrilateral element for analysis of plate bending. In: Proceedings of the 2nd Conference on Matrix Method in Structural Mechanic. Ohio, 1968. 399–440
- 11 Fraeijs de Veubeke B. A conforming finite element for plate bending. *Int J Solid Struct*, 1968, 4: 95–108
- 12 Stognier R H, Carey G F. C^1 macroelements in adaptive finite element methods. *Int J Numer Meth Eng*, 2007, 70: 1076–1095
- 13 Peano A. Conforming approximations for Kirchhoff plates and shells. *Int J Numer Meth Eng*, 1979, 14: 1273–1291
- 14 Chen J, Li C J. The cubic spline Hermite interpolation bases for thin plate bending quadrilateral elements (in Chinese). *Sci Sin Math*, 2015, 45: 1523–1536
- 15 Bogner F K, Fox R L, Schmit L A. The generation of interelement-compatible stiffness and mass matrices by the use of interpolation formulas. In: Proceedings of 1st Conference on Matrix Method in Structural Mechanics. Wright-Patterson Air Force Base, 1965. 397–443
- 16 Ferreira L J F, Bittencourt M L. Hierarchical high-order conforming C^1 bases for quadrangular and triangular finite elements. *Int J Numer Meth Eng*, 2017, 109: 936–964
- 17 Gopalacharyulu S. A direct method for the generation of shape functions of any desired continuity for rectangular finite elements. *J Struct Mech*, 1976, 4: 65–86
- 18 Watkins D S. On the construction of conforming rectangular plate elements. *Int J Numer Meth Eng*, 1976, 10: 925–933
- 19 Holdeman J T. A Hermite finite element method for incompressible fluid flow. *Int J Numer Meth Fluids*, 2010, 64: 376–408
- 20 Cowper G R, Kosko E, Lindberg G M, et al. Static and dynamic applications of a high-precision triangular plate bending element. *AIAA J*, 1969, 7: 1957–1965
- 21 Jeyachandrabose C, Kirkhope J. Explicit formulation for the high

- precision triangular plate-bending element. *Comput Struct*, 1984, 19: 511–519
- 22 Hrabok M M, Hrudey T M. A review and catalogue of plate bending finite elements. *Comput Struct*, 1984, 19: 479–495
- 23 Wanji C, Cheung Y K. Refined non-conforming quadrilateral thin plate bending element. *Int J Numer Meth Eng*, 1997, 40: 3919–3935
- 24 Tian Z, Wang D. A method for treating nonconforming thin plate bending problems. *Finite Elem Anal Des*, 2011, 47: 200–207
- 25 Sze K Y, Chow C L. An efficient hybrid quadrilateral Kirchhoff plate bending element. *Int J Numer Meth Eng*, 1991, 32: 149–169
- 26 Holdeman J T, Kim J W. Computation of incompressible thermal flows using Hermite finite elements. *Comput Method Appl Mech Eng*, 2010, 199: 3297–3304
- 27 Rückert J, Meyer A. C^1 -continuous FEM for Kirchhoff plates and large deformation. *Z Angew Math Mech*, 2015, 95: 200–214
- 28 Ivannikov V, Tiago C, Pimenta P M. Generalization of the C^1 TUBA plate finite elements to the geometrically exact Kirchhoff-Love shell model. *Comput Method Appl Mech Eng*, 2015, 294: 210–244
- 29 Lesičar T, Sorić J, Tonković Z. Large strain, two-scale computational approach using C^1 continuity finite element employing a second gradient theory. *Comput Method Appl Mech Eng*, 2016, 298: 303–324
- 30 Chen J, Li C J. A quadrilateral spline element for couple stress/strain gradient elasticity. *Comput Struct*, 2014, 138: 133–141
- 31 Zienkiewicz O C, Taylor R L, Zhu J Z. The Finite Element Method: Its Basis and Fundamentals. Oxford: Elsevier, 2013. 545–570
- 32 Henshell R D, Walters D, Warburton G B. A new family of curvilinear plate bending elements for vibration and stability. *J Sound Vib*, 1972, 20: 381–397
- 33 Cirak F, Ortiz M, Schröder P. Subdivision surfaces: A new paradigm for thin-shell finite-element analysis. *Int J Numer Meth Eng*, 2000, 47: 2039–2072
- 34 Gordon W J. Blending-function methods of bivariate and multivariate interpolation and approximation. *SIAM J Numer Anal*, 1971, 8: 158–177
- 35 Dhatt G, Touzot G, Lefrançois E. Finite Element Method. Hoboken: John Wiley & Sons, 2012. 136–137
- 36 Xing Y, Liu B. High-accuracy differential quadrature finite element method and its application to free vibrations of thin plate with curvilinear domain. *Int J Numer Meth Eng*, 2009, 80: 1718–1742
- 37 Timoshenko S P, Woinowsky-Krieger S. Theory of Plates and Shells. Singapore: McGraw-Hill, 1959. 313–314
- 38 Ramakrishnan R, Kunukkasseri V X. Free vibration of stiffened circular bridge decks. *J Sound Vib*, 1976, 44: 209–221
- 39 Kim C S, Dickinson S M. On the free, transverse vibration of annular and circular, thin, sectorial plates subject to certain complicating effects. *J Sound Vib*, 1989, 134: 407–421
- 40 Houmat A. A sector fourier p-element applied to free vibration analysis of sectorial plates. *J Sound Vib*, 2001, 243: 269–282